Wideband Multifunctional Bessel Beams by High Efficiency Spin-Decoupled Metasurface for Near field Applications

Hui-Fen Huang* and Chu-Xin Zheng

School of Electronic and Information Engineering, South China University of Technology, Guangzhou 510641, China

ABSTRACT: This paper develops a wideband spin-decoupled unit cell to form high efficiency wideband spin-decoupled metasurface (MTS), which can achieve more versatile Bessel beams with independent control of the beam direction, polarization, and Orbital angular momentum (OAM) mode for near field applications. The MTS is designed for wideband dual Bessel beams: Beam-I (RHCP, $\theta_1 = 30°$, $\varphi_1 = 180°$, $l = 1$), Beam-II (LHCP, $\theta_2 = 30°$, $\varphi_2 = 0°$, $l = 0$), where φ and θ are the azimuth and elevation angles, respectively; l is the OAM mode, and RHCP (LHCP) represents the right (left) hand circular polarization. Compared with conventional phase gradient MTSs, the proposed MTS achieves more versatile functionalities and better performance: wideband (35.3%), dual Bessel beams, circular polarization (CP), high aperture efficiency (AE) 40%, carrying OAM modes, high ratio of non-diffraction distance/aperture size (6.41), high conversion efficiency for Bessel beams (33%), and high OAM purity (78%–99%). Simulated and measured results agree well, and validate the design method. The proposed unit cell can be used to design other high performance multifunctional Bessel beams. The designed Bessel beams have potential applications in dense channel high capacity communication, efficient wireless power transfer, high-resolution imaging, medical treatment.

1. INTRODUCTION

OAM vortex electromagnetic wave [1] was first explicitly demonstrated by Allen et al. in 1992 which is characterized by helical phase structures, hollow-core intensity distributions, and intriguing infinite orthogonal OAM modes l. The infinite orthogonal modes have great potential in next generation large capacity wireless communications [2]. The spiral phase wavefront of OAM wave has the following special functions that traditional beams do not possess: (i) Azimuth detection ability, thereby achieving high resolution imaging [3]. (ii) Improving the medical diagnostic ability of some diseases, such as tumors due to the ability of measuring micrometer level cells [4]. (iii) The rotating speed detection of highrotating speed objects [5].

Bessel beam discovered by Durnin et al. in 1987 [6] is well known for its nondiffraction property along the radiation direction. The diffraction-free and self-reconstruction properties make the Bessel beam attractive in widespread applications, such as high-speed Line-of-sight short-range communication, efficient wireless energy transmission, medical imaging, and medical hyperthermia [7].

The Bessel OAM beam combines Bessel and OAM technologies, and is beneficial from the combination of infinite orthogonal modes and non-diffractive beam in near field region. The Bessel OAM beam contributes to the exploration of new dimensions in the near field region, further enriching the imaging, communication, and other near-field applications. So developing a multifunction high efficiency Bessel OAM beam generator is the key to drive the new dimensions [8].

MTS has the following obvious advantages: low profile, low loss, high gain, and remarkable capability of modulating EM waves. Recently, MTS has become a hot topic [9–12]. There are two representative approaches to manipulate the phase shift of the unit cell, namely Pancharatnam-Berry (PB) phase and propagation phase. Ref. [13] proposed a Pancharatnam-Berry metasurface to generate a left-hand circularly polarized OAM by a right-hand circularly polarized wave, which has the advantages of high gain and wide bandwidth. Several MTSs for generating multifunctional Bessel beams have been developed: Generation of multiple linear polarization (LP) pseudo Bessel beams with accurately controllable propagation directions and high efficiency using a propagation phase metasurface, which can independently manipulate the phases of the two orthogonal components (ϕ_x and ϕ_y) of the x-polarized and y-polarized waves, generation of a Bessel vortex beam carrying multiple OAM modes through a propagation phase MTS in the radio frequency domain [14], the fullspace Bessel beam modulator based on Pancharatnam-Berry (PB) phase MTS with dual CP [15], and generation of polarization rotation function Bessel beams based on all-dielectric PB phase MTS [16].

However, MTSs with PB (or propagation) phase alone have the following limitations: (i) PB (or propagation) phase alone can only control circular polarization (CP) (or LP). (ii) The phase controls for left hand circular polarization (LHCP) and right hand circular polarization (RHCP) incidences by PB phase MTS are exactly opposite and cannot independently control, that is, dual-CP incidence waves are coupled. (iii) The phase for elliptical polarization incidence cannot be controlled by MTS with propagation phase or PB phase alone. These limitations make the multifunctional MTSs unable to give full play to more

---

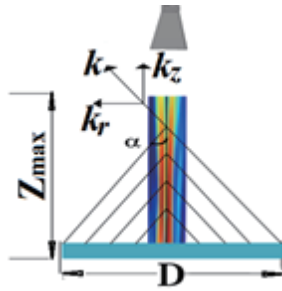* Corresponding author: Hui-Fen Huang (huanghf@scut.edu.cn).

47

FIGURE 1. Schematic diagram of generating Bessel beam through finite aperture.

FIGURE 2. The system diagram for dual Bessel beams.

versatility. Spin decoupled phase gradient MTS is the solution. Devlin et al. [17] integrated both PB and propagation phases, which can independently control the phase of dual-CP, or even any pair of orthogonal polarizations, which means that any pair of orthogonal polarizations is decoupled (namely spin-decoupled). Spin-decoupled unit cell improves degree of freedom in multifunctional design and can achieve more versatile functionalities and better performance. For example, the PB phase MTS is under dual CP incidences, if the OAM mode for RHCP is $l_r = 2$, then the OAM mode for LHCP must be $l_l = -2$. However, when the spindecoupled MTS is under dual CP incidences, any OAM mode for RHCP and LHCP can be generated, such as $l_r = 2$ and $l_l = 1$. Some works have been published: spin-decoupled MTS for simultaneous detection of spin and OAM via momentum transformation [18–22]. However, to the knowledge of the authors, there is no Bessel beams generated by spin-decoupled MTS.

In this paper, spin-decoupled multifunctional MTS is researched for achieving more versatile Bessel beams for more multifunctional near field applications. As an example, wideband dual Bessel OAM beams with independent control of the beam direction, polarization, and OAM mode are generated. Compared with published Bessel beams by conventional MTSs, the generated Bessel beams have the following advantages simultaneously: wideband (35.3%), dual Bessel beams, CP, high AE 40%, carrying orbital-angular-momentum modes, high ratio of non-diffraction distance to aperture size (6.41), high conversion efficiency for Bessel beams (33%), and high OAM purity from 78%–99%. The paper is organized as follows. The Bessel OAM beam design principle is in Section 2. Section 3 shows simulated and measured results, and Section 4 is conclusion.

2. DESIGN PRINCIPLE

Figure 1 is the schematic diagram for generating Bessel beam. It consists of two parts: the horn feeder and the MTS located in xoy plane at $z = 0$, and the coordinate origin is in the center of the MTS. The spherical wave from the horn feeder is converted into a non-diffracted Bessel beam by the MTS. α, D, and Z_{max} are the convergent angle, the antenna aperture, and 3 dB non-diffraction distance, respectively, as shown in Fig. 1.

2.1. Bessel Beams
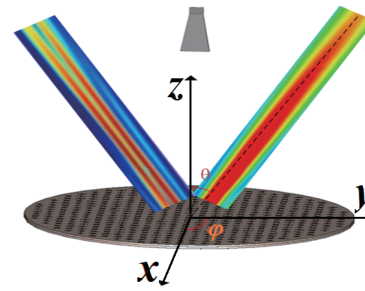
In the cylindrical coordinate system, a scalar solution of the wave equation propagating along the z-axis in free space can be represented by the cylindrical coordinate system (r, θ, z) as in [21]

$$E(r, \varphi, z, t) = 2J_m(k_r r) \exp(ik_z z + im\varphi - i\omega t) \quad (1)$$

where m represents the order of the Bessel function, and k_z and k_r represent the longitudinal and transverse wave vectors, respectively. When $m \neq 0$, "$m\varphi$" represents the Bessel beam carrying OAM wave with mode $l = m$. When $m = 0$, Equation (1) represents zero order Bessel beam as follows:

$$E(\rho, z, t) = \exp(i(k_z z - \omega t))J_0(K_r \rho) \quad (2)$$

where k_r and k_z are the radial and longitudinal components of the wave vector k in free space, respectively. The relationship among k_z, k, and k_r is as follows [22].

$$k_r = \frac{2\pi}{\lambda} \sin \alpha = \sqrt{k^2 - k_z{}^2} \quad (3)$$

where λ is the operating wavelength. The relationship among α, D, and Z_{max} is as follows [23]:

$$k_r = \frac{D/2}{\tan \alpha} \quad (4)$$

To generate a Bessel beam, parameters α and Z_{max} are required to be set first, and D is determined from (4). Theoretically, Z_{max} should be smaller than the radius of the near-field region. That is, $Z_{max} < 2D^2/\lambda$, Then the valid range of convergent angle α is

$$\frac{\lambda}{4D} < \sin \alpha \leq 1 \quad (5)$$

2.2. Phase Compensation Principle for Bessel Beam

In this paper, the Bessel beams are generated by phase gradient reflective MTS. The design principle of the unit cell for generating the Bessel beams is explained as follows.

The compensated phase $\Phi(x, y)$ of the unit cell in the MTS at position $(x, y, 0)$ satisfies the phase distribution for generating desired Bessel OAM beam (θ, φ, l).

There are several steps to calculate the required Φ:

$$\Phi = \Phi_1 + \Phi_2 + \Phi_3 \quad (6)$$

48

where Φ_1 is the compensated phase from the spherical wave to the plane wave, and

$$\Phi_1(x,y) = \frac{2\pi}{\lambda} H(x,y) \qquad (7)$$

where $H(x,y)$ is the distance between the position of unit at (x,y) and the phase center of the horn. Φ_2 is the compensated phase for the beam deflected direction:

$$\Phi_2(x,y) = -\frac{2\pi}{\lambda}(x\sin\theta\cos\varphi + y\sin\theta\cos\varphi) \qquad (8)$$

Φ_3 is the compensated phase shift to obtain Bessel beam:

$$\Phi_3(x,y) = \frac{2\pi}{\lambda}\left(\sqrt{x^2+y^2}\sin\alpha + l\arctan(y/x)\right) \qquad (9)$$

2.3. Design Principle for Spin-Decoupled Unit Cell

The spin decoupled unit cell is used to implement the phase compensation at $(x,y,0)$ calculated by (6)–(9). Assume that the incident and reflected electric field vectors are E_i and E_r, respectively. The vectors E_i and E_r consist of two orthogonal CP components, which can be written as the following forms:

$$E_i = (E_{iL}, E_{iR})^T$$
$$E_r = (E_{rL}, E_{rR})^T \qquad (10)$$

where the subscripts L and R represent LHCP and RHCP, respectively. When the reflective MTS is excited by a normal incident electromagnetic wave, the Jones matrix J of the MTS is $J = \begin{pmatrix} J_{LL} & J_{LR} \\ J_{RL} & J_{RR} \end{pmatrix}$. Then the reflective wave by the MTS is as follows:

$$\begin{pmatrix} E_{rL} \\ E_{rR} \end{pmatrix} = \begin{pmatrix} J_{LL} & J_{LR} \\ J_{RL} & J_{RR} \end{pmatrix} \begin{pmatrix} E_{iL} \\ E_{iR} \end{pmatrix} \qquad (11)$$

where J_{LL}, J_{LR}, J_{RL}, and J_{RR} represent the reflection coefficient components, and the first and second subscripts indicate the polarization states of the reflective and incident waves, respectively.

The reflection matrix J of the MTS can be written as [20]:

$$J = \begin{pmatrix} J_{LL} & J_{LR} \\ J_{RL} & J_{RR} \end{pmatrix} = \begin{pmatrix} \beta e^{-i2\zeta} & \delta \\ \delta & \beta e^{i2\zeta} \end{pmatrix} \qquad (12)$$

and $\beta = (R_x e^{i\phi_x} + R_y e^{i\phi_y})/2$, $\delta = (R_x e^{i\phi_x} - R_y e^{i\phi_y})/2$.

$R_{x(y)}$ and $\phi_{x(y)}$ are the reflection amplitude and reflection phase of the $x(y)$ polarized wave, respectively. ζ is the rotation angle of the unit, namely PB phase. For an ideal MTS (lossless, matching, and reciprocal) formed by units with X-axis or Y-axis symmetry, $|R_x| = |R_y| \approx 1$, $\phi_x - \phi_y = \pi$, and the cross-CP is suppressed. The John matrix J can be simplified as:

$$J = \begin{pmatrix} e^{-i2\zeta} & 0 \\ 0 & e^{i2\zeta} \end{pmatrix} \qquad (13)$$

From (12) and (13), the following relationship among the phases $\phi_{LL(RR)}$, $\phi_{x(y)}$, and ζ is obtained:

$$\phi_{LL} = \phi_x - 2\zeta \qquad (14)$$
$$\phi_{RR} = \phi_x + 2\zeta \qquad (15)$$

From (14) and (15), there is no longer any exactly opposite control between ϕ_{LL} (for LHCP) and ϕ_{RR} (for RHCP). ϕ_{LL} and ϕ_{RR} can be independently controlled, that is, dual-CP incident waves are decoupled. The unit cell forming the MTS is called spin-decoupled unit cell and should integrate both the propagation phase (ϕ_x and ϕ_y) and the PB phase (ζ). According to (14) and (15), ζ is obtained:

$$\zeta = \frac{\phi_{RR} - \phi_{LL}}{4} \qquad (16)$$

Then from (14)–(16), the propagation phases ϕ_x and ϕ_y are derived as follows:

$$\phi_x = \frac{\phi_{RR} + \phi_{LL}}{2} \qquad (17)$$

$$\phi_y = \frac{\phi_{RR} + \phi_{LL}}{2} - \pi \qquad (18)$$

In this paper, the spin decoupled unit cells are used to form the phase gradient reflective spin-decoupled MTS, which can generate multifunctional Bessel beams with the independent control of dual-CP incidence waves. Assume that the MTS is designed under LP incidence, because LP wave can be decomposed into two equal LHCP and RHCP waves, so both the LHCP and RHCP excitations are done simultaneously. According to (13), two co-polarized reflected beams LHCP (l_1, θ_1, ϕ_1) and RHCP (l_2, θ_2, ϕ_2) are generated. The geometry parameters $lx(y)$ and ζ are used to control the compensated phase of the unit cell, and other geometry parameters are fixed. Five steps for designing the unit cell are as follows. First, according to (6)–(9), the required compensated phase for the unit cell is calculated. Second, the required compensated phase is implemented by the spin-decoupled unit cell, that is $\phi_{LL} = \zeta + \phi_x + \phi_y$. Third, according to (16)–(18), the propagation phase ϕ_x (or ϕ_y) is controlled by the geometry parameter $lx(y)$. According to Fig. 4, the unit cell geometry parameter $lx(y)$ is determined, and other geometry parameters are fixed. Fifth, according to the phase distribution maps in Fig. 5, the phase gradient reflective spin-decoupled MTS is designed.

3. MTS DESIGN

The system diagram shown in Fig. 2 consists of a horn and the proposed reflective spin-decoupled MTS, which is excited by normal incidence from a y-polarized horn. All simulated results are by CST Microwave Studio.

3.1. Spin-Decoupled Unit Design

The proposed spin-decoupled unit shown in Fig. 3 consists of three metal layers separated by two $F4B$ substrate layers with thickness $1.5\,\text{mm}$ and dielectric constant 2.65. The top and middle metal patches have the same shape but different sizes,
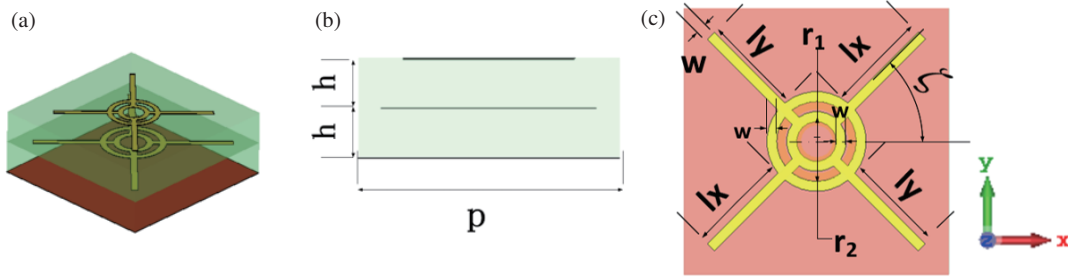
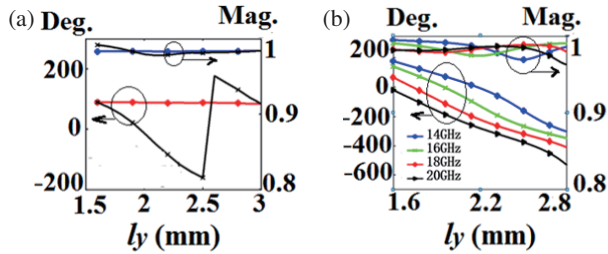FIGURE 3. The unit structure. (a) Simulation unit. (b) The left of unit. (c) The top of unit.

FIGURE 4. Reflection amplitude/phase *vs ly*: (a) *x* polarized wave or *y* polarized incidence at 17 GHz, (b) *y* polarized incidence for different frequency.
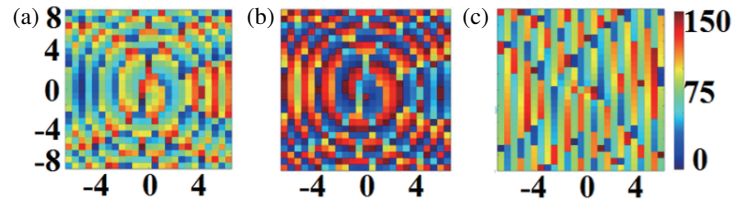

FIGURE 5. The phase distribution maps. (a) for ϕ_x. (b) for ϕ_y. (c) for ζ.

and the size of the top layer is 0.8 times that of the middle layer. The bottom metal layer is ground. All geometry parameters marked in Fig. 3 are as follows: $p = 8$ mm, $r_1 = 0.3$ mm, $r_2 = 0.7$ mm, $w = 0.2$ mm. The propagation phase $\phi_x(\phi_y)$ is controlled by $lx(ly)$, and the PB phase is controlled by the rotation angle ζ.

When $\zeta = 0°$, $lx = 2$ mm, Fig. 4(a) shows the curves of magnitude and phase of scattering parameter S_{11} *vs ly* for ly from 1.6 mm to 3 mm at 17 GHz. For y-polarized incidence, the simulated phase shift range can cover $360°$, and the S_{11} magnitudes are above 0.95. For x-polarized incidence, the magnitude (or phase) of the S_{11} keeps 0.96 (or $90°$) unchanged. Due to symmetry of the unit, the curve for reflection amplitude (or phase) of S_{11} vs lx for x-polarized incidence is similar to the curve in Fig. 4(a or b).

The curves of the magnitude and phase *vs ly* are shown in Fig. 4(b) at 14 GHz, 16 GHz, 18 GHz, and 20 GHz. The phase curves are parallel; the S_{11} amplitudes keep above 0.96 in the operation band; and wideband 35% is obtained.

3.2. Spin-Decoupled MTS Design

The proposed unit is used to form the spin-decoupled MTS with diameter $D = 16p$ for generating wideband high efficiency multifunctional Bessel beams with independent control of the beam direction, polarization, and OAM mode. As an example, the following dual Bessel beams are designed to validate the design technique: Beam-I (RHCP, $\theta_1 = 30°$, $\varphi_1 = 180°$, $l = 1$), Beam-II (LHCP, $\theta_2 = 30°$, $\varphi_2 = 0°$, $l = 0$). $Z_{max} < 2D^2/\lambda = 4.545$ m at 17 GHz, and here Z_{max} is set as 1 meter. PB phase ζ and the propagation phase (ϕ_x and ϕ_y) distribution maps calculated by (6)–(9) are shown in Figs. 5(a)–(c),

respectively. Then the corresponding geometry length (lx, ly) distribution maps in the MTS are obtained according to Fig. 4.

4. SIMULATED AND MEASURED RESULTS

Both the near-field and far-field have been simulated to verify the vortex property and diffraction free properties of Bessel beams. To validate the design, the prototype of the designed spin-decoupled MTS for dual Bessel beams has been fabricated. Figs. 6(a) and (b) are the prototypes of the top layer and the measurement environment, respectively. A KEYSIGHT E5071C Vector Network Analyzer (VNA) was used to test the Bessel beam E-field distribution. The simulated E-field amplitude distributions at 14 GHz, 17 GHz, and 20 GHz are shown in Fig. 7. The profile is nearly unchanged at different frequencies, which indicates the wideband characteristic of the spin-decoupled MTS. The simulated -3 dB non-diffraction distances (d) are 750 mm, 830 mm, and 700 mm at 14 GHz, 17 GHz, and 20 GHz, respectively, which approach the set non-diffraction distance 1000 mm. The ratios of d/D are 5.86, 6.41, and 5.47 at 14 GHz, 17 GHz, and 20 GHz, respectively.

Figures 8(a)–(c) are the simulated and measured E-field and phase distributions for Beam-I (RHCP, $\theta_1 = 30°$, $\varphi_1 = 180°$, $l = 1$) in the plane (300 mm away from the MTS along the propagation direction) at 14 GHz, 17 GHz, and 20 GHz. The helical phase pattern and zero-intensity area in the plane center are clearly recognized. The simulated and measured results are basically consistent.

The Bessel beam conversion efficiency (η) of the MTS can be defined as the ratio of Bessel beam power P_1 to the power P_0 emitted by the horn feeder. The integral plane S in Fig. 9 has a size of 100 mm $\times$ 100 mm. And the calculated maximum Bessel
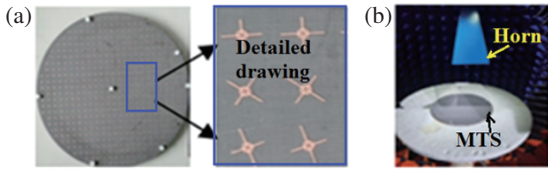
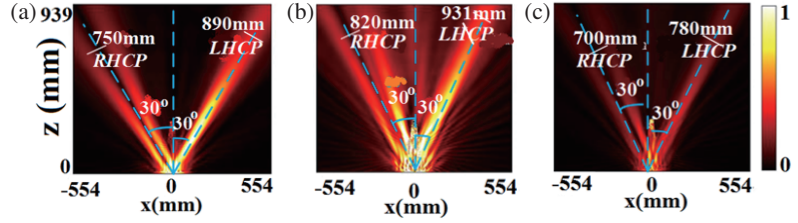FIGURE 6. (a) The prototypes of the metasurface. (b) The measurement environmen.

FIGURE 7. The simulated near-field in xoz plane. (a) 14 GHz. (b) 14 GHz. (c) 20 GHz.
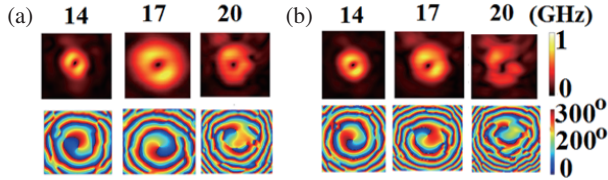

FIGURE 8. E-field and phase distributions in the plane (300 mm away from the MTS along the propagation direction) for Beam-I at 14 GHz, 17 GHz and 20 GHz. (a) Simulated. (b) Measured.
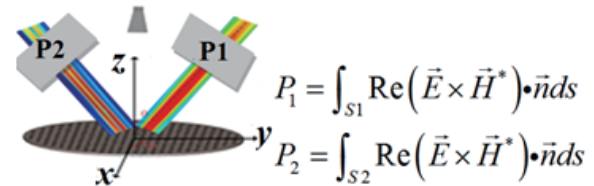

FIGURE 9. Schematic diagram of the beam conversion efficiency calculation method.
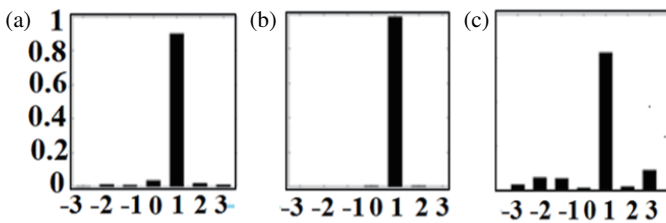
$$P_1 = \int_{S1} \mathrm{Re}\left(\vec{E} \times \vec{H}^*\right) \cdot \vec{n} ds$$

$$P_2 = \int_{S2} \mathrm{Re}\left(\vec{E} \times \vec{H}^*\right) \cdot \vec{n} ds$$

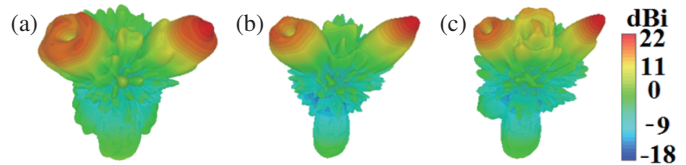FIGURE 10. The OAM spectrums. (a) at 14 GHz. (b) at 14 GHz. (c) at 20 GHz.

FIGURE 11. The far-field radiation patterns. (a) at 14 GHz. (b) at 14 GHz. (c) at 20 GHz.

TABLE 1. Comparison between the proposed design and recently published MTSs.

Ref.	bandwidth	Beam number	Polarized	Unit type	d/D	OAM mode l	η
[25]	10%	1	LP	Propagation	2.38	0	–
[26]	57.1%	2	LP	Propagation	1.23	0	37%
[14]	14%	1	LP	Propagation	–	1 or 2	–
This work	35.3%	2	LHCP, RHCP	spin-decoupled	6.41	1 and 0	40%

beam conversion efficiency is more than 40% at a transmission distance of 120 mm from the MTS by superimposing the efficiency of two beams. With the increase of the distance, the conversion efficiency decreases, and the conversion efficiency is greater than 30% until the distance is 300 mm.

The OAM spectrums are shown in Fig. 10. The purities for $l = 1$ at 14 GHz, 17 GHz, and 19 GHz are 92.41%, 99%, and 78%, respectively. High OAM mode purity is obtained in the operation band from 14 GHz to 20 GHz. The far-field radiation patterns under y-polarized incidence at 14 GHz, 17 GHz, and 20 GHz are shown in Fig. 11. Dual beams are generated: RHCP ($\theta_1 = 30°$, $\varphi_1 = 180°$, $l = 1$) and LHCP ($\theta_2 = 30°$, $\varphi_2 = 0°$, $l = 0$). The simulated beams agree well with the calculated results. Vortex beams are clearly observed for first order Bessel beams, and there is no vortex property for zero order

Bessel beams. The far-field gain is above 18 dBi in 14–20 GHz, and the simulated aperture efficiencies are 36.3%, 38.5%, and 37.2% at 14 GHz, 17 GHz, and 20 GHz, respectively. Because LP wave can be decomposed into two equal LHCP and RHCP waves, both the LHCP and RHCP excitations are done simultaneously.

Table 1 is a comparison with recently published Bessel beam MTSs in bandwidth, beam number, polarization, unit type, ration d/D, OAM mode, and conversion efficiency. Compared with [23], [24], and [25], the proposed MTS is spin decoupled with independent control of dual CP, higher d/D ratio 6.41, higher Bessel beam conversion efficiency 40%, and multifunction beams with independent control of the beam direction, polarization, and OAM mode.

5. CONCLUSION

This paper develops a high efficiency spin-decoupled MTS which is researched for wideband multifunctional Bessel beams with independent control of the beam direction, polarization, and OAM mode for near field applications. As an example, a spin-decoupled MTS is designed for wideband dual CP Bessel beams: Beam-I (RHCP, $\theta_1 = 30°$, $\varphi_1 = 180°$, $l = 1$), Beam-II (LHCP, $\theta_2 = 30°$, $\varphi_2 = 0°$, $l = 0$). Compared with recently published MTSs on Bessel beams, the proposed MTS is spin decoupled with dual CP, higher d/D ratio 6.41, higher Bessel beam conversion efficiency 40%, and multifunction beams with independent control of the beam direction, polarization and OAM mode. The developed design technique can be used in designing high efficiency MTSs in the near field application scenarios such as dense channel high capacity communication, high-resolution microwave imaging, near-field detection, efficient wireless energy transmission, and medical detection.

REFERENCES

[1] Allen, L., M. W. Beijersbergen, R. Spreeuw, and J. Woerdman, "Orbital angular-momentum of light and the transformation of laguerre-gaussian laser modes," *Physical Review A*, Vol. 45, No. 11, 8185–8189, Jun. 1992.

[2] Benassi, F., W. Fuscaldo, D. Masotti, A. Galli, and A. Costanzo, "Wireless power transfer in the radiative near-field through resonant bessel-beam launchers at millimeter waves," in *2021 IEEE Wireless Power Transfer Conference (WPTC)*, 1–4, IEEE, Jun. 2021.

[3] Zeng, Y., Y. Wang, Z. Chen, J. Zhang, and J. Zhang, "Two-dimensional OAM radar imaging using uniform circular antenna arrays," in *2020 14th European Conference on Antennas and Propagation (EuCAP 2020)*, 1–4, IEEE, Copenhagen, Denmark, Mar. 2020.

[4] Amphawan, A., A. Anwar, S.-K. Ong, J. Sutanto, T.-K. Neo, and K. Anwar, "Free-space optical space division multiplexing for smart healthcare," in *2022 8th Annual International Conference on Network and Information Systems For Computers (ICNISC)*, 527–532, IEEE, 2022.

[5] Xie, Q., T. Yu, Z. Tan, W. Xie, and G. Qin, "Rotational speed measurement under misalignment conditions based on rotational doppler effect," in *Aopc 2022: Advanced Laser Technology and Applications*, Vol. 12554, 129–134, SPIE, 2023.

[6] Durnin, J., J. J. Miceli, and J. H. Eberly, "Diffraction-free beams," *Physical Review Letters*, Vol. 58, 1499–1501, Apr. 1987.

[7] Feng, F., S. Goswami, S. Khan, and S. A. McAleavey, "Evaluating the feasibility of nondiffractive bessel beams for shear wave elasticity imaging: A simulation study," in *2020 IEEE International Ultrasonics Symposium (IUS)*, 1–4, IEEE, 2020.

[8] Zhang, D., J. Zhang, J. Liu, and X. Wang, "Topological transformation OAM based on metasurface generated bessel beam," in *2019 International Symposium on Antennas and Propagation (ISAP 2019)*, 1–2, IEEE, Xian, China, Oct. 2019.

[9] Wang, L., Y. Yang, S. Li, L. Deng, W. Hong, C. Zhang, J. Zhu, and D. McGloin, "Terahertz reconfigurable metasurface for dynamic non-diffractive orbital angular momentum beams using vanadium dioxide," *IEEE Photonics Journal*, Vol. 12, No. 3, 1–12, Jun. 2020.

[10] Xu, B., C. Wu, Z. Wei, Y. Fan, and H. Li, "Generating an orbital-angular-momentum beam with a metasurface of gradient reflective phase," *Optical Materials Express*, Vol. 6, No. 12, 3940–3945, Dec. 2016.

[11] Qin, F., L. Wan, L. Li, H. Zhang, G. Wei, and S. Gao, "A transmission metasurface for generating OAM beams," *IEEE Antennas and Wireless Propagation Letters*, Vol. 17, No. 10, 1793–1796, Oct. 2018.

[12] Guo, Y., S. Zhang, M. Pu, Q. He, J. Jin, M. Xu, Y. Zhang, P. Gao, and X. Luo, "Spin-decoupled metasurface for simultaneous detection of spin and orbital angular momenta via momentum transformation," *Light-science & Applications*, Vol. 10, No. 1, 63, Mar. 2021.

[13] Gao, X., L. Tang, X. Wu, and S. Li, "Broadband and high-efficiency ultrathin pancharatnam-Berry metasurfaces for generating X-band orbital angular momentum beam," *Journal of Physics D: Applied Physics*, Vol. 54, No. 7, 075104, Feb. 2020.

[14] Feng, Q., Y. Lin, M. Shan, Y. Mu, and L. Li, "Generation and measurement of a bessel vortex beam carrying multiple orbital-angular-momentum modes through a reflective metasurface in the RF domain," *Physical Review Applied*, Vol. 15, No. 6, 064044, 2021.

[15] Zhu, C., H. Liang, F. Wang, F.-Y. Wen, and J. Huang, "The full-space bessel beam modulator based on pancharatnam-berry metasurface," in *2019 Photonics & Electromagnetics Research Symposium-Fall (PIERS-Fall)*, 507–513, IEEE, 2019.

[16] Zhi, J., Y. Guo, B. Hu, X. Wang, X. Yu, Z. Qiu, K. Huang, M. Yao, and B. Xu, "Generation of polarization rotation function bessel beams based on all-dielectric metasurfaces," *Optics Communications*, Vol. 550, 130014, Jan. 2024.

[17] Devlin, C., A. Ambrosio, N. A. Rubin, J. B. Mueller, and F. Capasso, "Arbitrary spin-to-orbital angular momentum conversion of light," *Science*, Vol. 358, 896, 2017.

[18] Zhu, L. and J. Wang, "Arbitrary manipulation of spatial amplitude and phase using phase-only spatial light modulators," *Scientific Reports*, Vol. 4, No. 1, 7441, Dec. 2014.

[19] Huang, H.-F. and J.-J. Ye, "Reconfigurable reflective multifunction OAM metasurface based on spin-decoupling," *Optics Letters*, Vol. 47, No. 19, 4873–4876, Oct. 2022.

[20] Ding, G., K. Chen, X. Luo, J. Zhao, T. Jiang, and Y. Feng, "Dual-helicity decoupled coding metasurface for independent spin-to-orbital angular momentum conversion," *Physical Review Applied*, Vol. 11, No. 4, 044043, Apr. 2019.

[21] Xu, P., H. Liu, R. Li, K. Zhang, and L. Li, "Dual-band spin-decoupled metasurface for generating multiple coaxial OAM beams," *IEEE Transactions on Antennas and Propagation*, Vol. 70, No. 11, 10 678–10 690, Nov. 2022.

[22] Zheng, C., G. Wang, J. Li, J. Li, S. Wang, H. Zhao, M. Li, Z. Yue, Y. Zhang, Y. Zhang, and J. Yao, "All-dielectric metasurface for manipulating the superpositions of orbital angular momentum via spin-decoupling," *Advanced Optical Materials*, Vol. 9, No. 10, 2002007, May 2021.

[23] Liu, H., H. Xue, Y. Liu, and L. Li, "Generation of multiple pseudo bessel beams with accurately controllable propagation directions and high efficiency using a reflective metasurface," *Applied Sciences*, Vol. 10, No. 20, 7219, Oct. 2020.

[24] Zhong, Y. C. and Y. J. Cheng, "Ka-band wideband large depth-of-field beam generation through a phase shifting surface antenna," *IEEE Transactions on Antennas and Propagation*, Vol. 64, No. 12, 5038–5045, Dec. 2016.

[25] Chávez-Cerda, S., "A new approach to bessel beams," *Journal of Modern Optics*, Vol. 46, No. 6, 923–930, May 1999.

PIER Letters

[26] Huang, H. and X. Tang, "Wideband multiple bessel beams with desired directions and energy distribution proportion based on time reversal and genetic algorithm in microwave," *IEEE Transactions on Magnetics*, Vol. 59, No. 6, Jun. 2023.

[27] Shahmirzadi, A. V., Z. Badamchi, B. Badamchi, and H. Subbaraman, "Generating concentrically embedded spatially divided OAM carrying vortex beams using transmitarrays," *IEEE Transactions on Antennas and Propagation*, Vol. 69, No. 12, 8436–8448, 2021.